# Single-molecule imaging to characterise the transport mechanism of the Nuclear Pore Complex

Grace Jeremy[1], James Stevens[2], and Alan R. Lowe[1,2,3]*

[1]Structural & Molecular Biology, University College London, Gower Street, London, UK, WC1E 6BT
[2]Department of Biological Sciences, Birkbeck College, University of London, Malet Street, London, UK, WC1E 7HX
[3]London Centre for Nanotechnology, 17-19 Gordon Street, London, UK, WC1H 0AH

*Corresponding author: a.lowe@ucl.ac.uk

**Summary**

**In the eukaryotic cell, a large macromolecular channel, known as the Nuclear Pore Complex (NPC), mediates all molecular transport between the nucleus and cytoplasm. In recent years, single-molecule fluorescence (SMF) imaging has emerged as a powerful tool to study the molecular mechanism of transport through the NPC. More recently, techniques such as Single-Molecule Localisation Microscopy (SMLM) have enabled the spatial and temporal distribution of cargos, transport receptors and even structural components of the NPC to be determined with nanometre accuracy. In this protocol, we describe a method to study the position and/or motion of individual molecules transiting through the NPC with high spatial and temporal precision.**

**Key Words**

Nucleus, Nuclear Pore Complex, Single-Molecule Tracking, Super-resolution Microscopy

## 1. Introduction

**The Nuclear Pore Complex**

The eukaryotic cell contains an envelope bound nucleus, a structure facilitating the spatial and temporal partitioning of the genetic material and molecules critical to normal function. The movement of molecules, termed cargos, across the envelope is called nucleocytoplasmic transport. This process is key for regulating nuclear composition and gene expression. The Nuclear Pore Complex (NPC) is the major channel of passage between the nucleus and cytoplasm, facilitating passive transport of small cargo and the regulated transport of larger molecules. NPCs are formed from many copies of ~30 nucleoporin proteins (Nups), with a total of 500-1000 Nups forming a single NPC. "Barrier Nups", are found throughout the NPC channel structure and are comprised of phenylalanine-glycine rich repeat (FG) motifs [1]. These FG-Nups control the selective transport of large cargoes through the central channel of the NPC [2]. The FG motifs protrude into the central channel, generating a permeability

barrier which permits the unhindered passage of small, non-polar molecules (ions, metabolites) whilst occluding larger cargoes (macromolecules, proteins > 40KDa) [3].

Large cargoes destined for transport possess specific amino acid sequences or patches called nuclear localisation (NLS) signals [4]. These bind (via adaptor proteins) to Nuclear Transport Receptors (NTRs), such as Importin-beta (Impβ) [5]: proteins that facilitate transport by forming multiple interactions with the barrier Nups. Transport of Nup-interacting proteins is very efficient and greatly exceeds that of non-interacting proteins, with a translocation rate of $\sim 10^3$ s$^{-1}$ NPC$^{-1}$ [6]. The directionality of Impβ-dependant transport is controlled by a sharp spatial gradient of the GTPase Ran in either its GDP- or GTP-bound state [7,8]. RanGTP dominates the nuclear side whereas RanGDP is the prevalent cytoplasmic form. A typical import complex comprises Impβ, Impα and cargo. Upon reaching the nuclear face of the NPC, the Impβ binds RanGTP, promoting the release of cargo into the nucleus [9].

Many models of transport, with varying functional arrangements of the FG-nups, have been proposed. The permeability of the NPC could result from a physical barrier as proposed in the "selective phase" model, with barrier Nups interacting to form a size-selective mesh preventing the movement of larger cargoes [6]. Alternatively it could be energetic as in the "virtual-gate" model, occluding molecules that do not interact with the FG-repeats as they cannot overcome the entropic barrier formed by the dense FG-lining of the central channel [10]. Other studies suggest the FG-nups form a hydrogel through crosslinking interactions, and that this acts as a sieve permitting passage of NTR complexes [11,12]. Recent studies also suggest that a FG-nup meshwork is only partially stable, and that NTRs may influence inter-Nup interactions to permit the active movement of cargo [13,14]. However, despite the many theories, and a wealth of experimental data, the mechanism of translocation is still largely unresolved.

**Single-Molecule Imaging of the NPC**

In recent years, single-molecule fluorescence (SMF) imaging has emerged as a complimentary technique for studying the mechanism of the NPC. SMF microscopy is a highly specific and non-invasive imaging method, capable of visualising individual fluorophores conjugated to biological molecules of interest. As such it has been utilised, to great effect, to study individual transport reactions in cells in real-time. Several different experimental geometries have been established to enable quantitative measurements of either the transport reaction, or of the structural arrangement of components of the NPC. Typically, these experiments use *Digitonin* permeabilised mammalian cells [15] and a reconstituted recombinant import system, including a fluorescently labelled molecule of interest (e.g. NTR, cargo or component of the NPC itself).

Total Internal Reflection Fluorescence (TIRF) microscopy is often used to perform SMF imaging experiments due to the enhanced signal-to-noise ratio (S/N), but this limits the illumination volume to only ~100 nm above the coverglass surface. In most cases, the nucleus, and hence the NPCs are located above this illumination volume, therefore many alternative strategies have been developed to directly visualise the basal and equatorial planes of the nucleus.

For example, widefield and narrowfield (enhancing the S/N) epifluorescence have been used to measure NTR transport times and the localisation of NTR-NPC interaction sites within single NPCs [16], as well as the effect of NTR concentration on transport kinetics [17]. These NTR dwell time and binding site distribution measurements have aided determination of likely transport models and lead to the suggestion that multiple transport pathways are present in a single NPC [18,19]. Highly inclined and laminated optical sheet (HILO) microscopy further increases S/N, enabling measurement of cargo-NTR dissociation constants and quantification of the number of NTRs present at single NPCs [20]. Single-Point Edge-Excitation subDiffraction (SPEED) microscopy can also improve S/N, by limiting the illumination volume to a single NPC. This has been used to observe transient NTR-cargo-Nup interactions [21] suggesting that spatially distinct routes exist for facilitated and passive transport [22].

In addition, alternative fluorescent probes have been utilised to measure different aspects of the transport reaction. For example cargo tracking experiments utilising semiconductor nanoparticles have visualised transport of large cargos through the NPC channel, exploiting the photostability and size of the probes [23]. Dye pairs have been used to perform single-molecule Förster Resonance Energy Transfer (smFRET) experiments, revealing the mechanism of impα-cargo dissociation [24].

Most recently, "super-resolution" SMLM imaging (in particular, techniques such as PALM [25], STORM [26] and *d*STORM, [27]) has been used to precisely localise many molecules within NPCs. For example HILO-*d*STORM has enabled precise visualisation of the spatial distribution of NTRs, and inter-NPC variability under different conditions [13]. *d*STORM has also been utilised independently [28] and combined with correlative electron microscopy [29] to assess the organisation of structural domains within the NPC [30].

In this protocol, we will describe, in detail, our most current workflow for imaging the location and/or motion of cargos and NTRs using SMLM imaging and single-particle tracking (SPT). The same basic protocol can be used to perform either type of experiment, with the major experimental difference being whether the sample is fixed (SMLM, *d*STORM) or live (SPT), and how the data are processed.

Our workflow comprises several steps:

1. Expression and purification of recombinant transport receptors and cargos
2. Chemical labelling of the NTRs or cargo with fluorescent moieties
3. Digitonin permeabilisation of cells and addition of recombinant transport system
4. Single-molecule imaging using highly inclined illumination (HILO)
5. Single Particle Tracking or Localisation Microscopy (e.g. *d*STORM)
6. Data analysis to generate composite maps of the NPC

## 2. Materials

### 2.1 - Protein Expression and Purification

1. *Escherichia coli* cells (OneShot BL21 (DE3), Life Technologies)
2. Expression plasmid for His$_6$-tagged cargo, NTRs or Ran
3. 2L LB medium with appropriate antibiotics
4. 1M IPTG
5. 5 ml HisTrap column (GE Healthcare)
6. Elution buffer containing Imidazole: 3 mM Imidazole, 2 mM DTT in PBS, pH 7.4

### 2.2 - Labelling of the NTRs or cargo with fluorescent moieties

1. Gene encoding photoactivatable fluorescent protein (such as mEOS3)
2. Chemical dye such as the N-hydroxysuccinimidyl ester of AlexaFluor 647 (Life Technologies A-20006)
3. Nanoparticles such as Amino (PEG) Quantum Dots (Life Technologies Q21501MP)

### 2.3 – Preparation of cells for imaging

1. HeLa cells
2. 75 cm$^2$ tissue culture flasks
3. 10 ml of growth media: 1:1 solution of Dulbecco's Modified Eagle Medium and F12 (Gibco), 10% foetal calf serum (FCS) (Gibco) and 1% penicillin/streptomycin (Gibco)
4. Incubator (37°C, 5% (v/v) CO$_2$).
5. HBSS (Gibco)
6. 0.05% EDTA/trypsin (Gibco)
7. Glass bottom dishes (Ibidi, μ-Dish $^{35\ mm,\ high}$)

### 2.4 Recombinant transport assay

1. Phosphate Buffered Saline (PBS): 50 mM, pH 7.4
2. Permeabilisation buffer (PB): 50 mM HEPES pH 7.3, 50 mM KOAc, 8 mM MgCl$_2$
3. Digitonin-Permeabilisation buffer (DPB): PB plus 0.1 mM Digitonin in DMSO, 80 μM ATP, 80 μM GTP, 3.2 mM Creatine phosphate and 40 Units Creatine Kinase in PBS

4. Transport buffer (TB): 20 mM HEPES pH 7.3, 110 mM KOAc, 5 mM NaOAc, 2 mM Mg(OAC)$_2$, 4 mM DTT, pH 7.3

5. Import Mix (IMx): 1.5 μM Impβ, 8 μM ATP, 8 μM GTP, 320 μM Creatine phosphate, 4 Units Creatine Kinase in PBS, 2 μM DTT, 1X TB, in dH$_2$O

6. Ran Mix (RMx): 0.03 μM RanGAP, 4 nM RanBP, 10.3 μM GDP, 0.06 μM NTF2

7. Energy Mix (EMx): 0.75 mM ATP, 0.75 mM GTP, 15 mM creatine phosphate, 0.075 mg.ml$^{-1}$ creatine kinase in HEPES, 0.075 mM DTT, 0.075 mM Mg(OAC)$_2$, pH 7.5

8. Fluorescent beads (0.1 μm TetraSpeck Fluospheres, Life Technologies) as fiducial markers for drift correction.

9. Imaging buffer 100 mM mercaptoethylamine, 0.5 mg/ml glucose oxidase, 0.2% vol/vol catalase and 10% wt/vol D-Glucose in PBS pH 7.4.

10. Nail varnish and coverglass, to seal the chamber for SMLM.


## 2.5 – Single-Molecule Imaging instrumentation

We perform single-molecule using a custom built microscope, based on an Olympus IX81 base (**Figure 2**). The system is set-up to allow epifluorescence, TIRF or inclined illumination of the sample. Inclined illumination schemes (including HILO) can be used to improve the S/N ratio of the imaging, by reducing the illumination of molecules above and below the focal plane of interest. TIRF illumination cannot be employed since the NPCs are typically located above the shallow (~100 nm) evanescent field of illumination. The system comprises the following features:

1. Four lasers (100 mW 405 nm Coherent Obis, 100 mW 488 nm Coherent Sapphire, 150 mW 561 nm Coherent Sapphire and a 150 mW Toptica iBeam Smart, **See Note 1**), each with their own shutter control, are expanded to the same diameter and combined using a series of dichroic mirrors (Semrock LaserMUX) into a single free-space beam. Half-wave plates were used to adjust the polarisation before passing the beams through an Acousto-Optical Tunable Filter (AOTF, AA Optoelectronics, France) to quickly modulate laser power. The combined beams are again expanded and launched into a single-mode optical fibre (Thorlabs PM-S405-XP) using an inexpensive Olympus 10X (0.1 N.A. air) objective lens.

2. The output of the optical fibre is collimated using an achromatic parabolic mirror collimator and passed through a quarter-wave plate to circularly polarise the beam to prevent orientation specific excitation of fluorophores. The free beam is then passed through a "TIRF lens" (Thorlabs AC254-200-A-ML), focussing the expanded beam, via a multi-edge dichroic filter (Semrock Di01-R405/488/561/635-25x36), directly onto the back focal plane of an apochromatic Olympus 100x 1.49 N.A. objective lens. This entire subsystem can be mounted on a translation stage to adjust the translation of the beam across the back focal plane of the objective, and therefore adjust the inclination of the beam at the sample plane (**See Note 2**).

3. Actively cooled EMCCD cameras (Andor iXon Ultra DU-897U-CS0-#BV) are coupled to the camera port of the microscope via an additional 1.5X magnifying relay. The magnifiying relay ensures that optimal Shannon-Nyquist sampling is achieved in the final image. An additional dichroic mirror in the Fourier plane of the relay can be used to simultaneously image a second colour on the second camera. Full frame camera acquisition is performed at 33 Hz (corresponding to an exposure time of 30 ms).

4. Appropriate bandpass filters (e.g. Semrock FF01-520/35-25 for GFP) are mounted in the Fourier space before of each camera, in order to select the emission of the fluorescent molecule used.

5. The laser shutters, AOTF and camera firing are synchronised using the external clock of a Data Translation DT9834 data acquisition module.

6. Sample positioning is controlled via a manual micrometre stage coupled with a 200 μm range three-axis nanopositioning stage (Physik Instrumente P-545.3R7).

Focal drift can be minimised using a focus-locking system (**See Note 3**). Here we present a design for a simple, low-cost, home-built focus-locking system based on total internal reflection of a near-IR laser off of the coverglass, with the return beam monitored by a linear two-axis position sensitive detector (**Fig 3**). A simple low-noise bipolar power supply (modified from: http://tangentsoft.net/elec/vgrounds.html) can be created for powering the lateral effect sensor, which can then be read out using an Arduino or high-resolution A/D converter. A PID (Proportional, Integral, Differential) control loop drives the nanopositioner to correct and maintain the sample position and account for focus drift. Translational drift is corrected post acquisition. The components required for the focus lock system are:

1. Data Translation DT9834 Analogue to Digital converter
2. Thorlabs PDP90A Lateral Effect Sensor
3. Thorlabs 785nm laser (CPS780S)
4. 10V Power supply (we used an Isotech IPS303DD DC Power supply)
5. Texas Instruments TLE2426IP Rail Virtual Ground with Noise Reduction
6. Hirose HR10A-7R-6S(73) 6-pin Circular Connector
7. Panasonic EEU-FC1V221L 220uF Aluminium Electrolytic Capacitor
8. Panasonic ECQ-V1H105JL 1uF Film Capacitor
9. IR Dichroic mirror and IR notch filter (Semrock FF750-SDi02-25x36)

Pins 4,5 and 6 of the PDP90A are connected to the +5v, Ground and -5v of the bipolar supply respectively. Pins 1,2 and 3 (X-position, $\Delta x$, Y-position, $\Delta x$ and Sum voltage, S) are connected to the analogue inputs of either the DAQ or an Arduino (via an additional circuit). The return beam position is calculated using the sensor size ($L_x = L_y$ = 10 mm) as:

$$x = \frac{L_x \cdot \Delta x}{2S}, y = \frac{L_y \cdot \Delta y}{2S}$$

This return beam directly reports on the distance (separation) between the objective lens and the glass/water interface of the sample and can be used to correct/maintain the focus in real time.

## 2.6 Software

Software is required to localise, (track, if live) and align the single-molecule trajectories from the camera acquisition data. In practice many software packages are available to localise molecules and perform drift correction (e.g. QuickPALM [31], ThunderSTORM [32], MLE [33]) using a Gaussian approximation of the Point Spread Function (PSF). Tracking can be performed using open source software such as the Crocker and Grier particle tracking code (http://physics.nyu.edu/grierlab/software.html) [34] or TrackMate (http://fiji.sc/TrackMate) [35].

In practice, we use a mixed C++/Python software library, ImPy, developed in-house, to localise, drift-correct and track molecules, and a simple MATLAB interface to perform subsequent single-particle data analysis. The latest version of the source code for the image analysis tools can be downloaded from *github*:

```
git clone https://github.com/quantumjot/impy-tools
git clone https://github.com/quantumjot/NPC-localisation-tools
```

## 3. Methods

### 3.1 - Protein Expression and Purification

*Escherichia coli* cells can be transformed with the appropriate plasmid for a His$_6$-tagged cargo, NTRs or Ran, grown up in 1-2L cultures induced with of 1M IPTG overnight at 37°C. Lyse cells with a cell homogeniser, and purify the protein using a 5 ml HisTrap column, eluting with a gradient of elution buffer containing Imidazole (300 mM Imidazole, 2 mM DTT in PBS, pH 7.4).

### 3.2 Labelling of proteins

Proteins can either be expressed as fusion proteins containing a photo-convertible fluorescent protein (e.g. mEOS3) or chemically labelled using fluorescent dyes such as an N-hydroxysuccinimidyl ester of AlexaFluor 647 as per the manufacturers instructions (**See Note 4**).

### 3.3 – Preparation of cells for imaging

1. Grow HeLa cells in 75 cm$^2$ tissue culture flasks containing 10 ml of growth media in an incubator (37°C, 5% (v/v) $CO_2$).

2. Once grown to approximately 80% confluence, aspirate the media from the flasks and wash cells with 5ml HBSS prior to incubation with 2 ml 0.05% EDTA/trypsin (5 min, 37°C, 5% (v/v) $CO_2$).

3. After detachment, add 7 ml HBSS/10% FCS and transfer to a 15 ml falcon tube for centrifugation (1200 g, 4°C, 5 min).

4. Aspirate the resulting supernatant before resuspending the cell precipitate in 5 ml HBSS/10% FCS. Seed the cells in 10 ml growth media at $2x10^6$ cells per flask.

5. Wash glass bottom dishes (Ibidi, $\mu$-Dish $^{35\text{ mm, high}}$) with 2 ml HBSS.

6. Seed dishes with HeLa cells (incubate in 2ml growth media at 37°C (5% (v/v) $CO_2$, for 24 h) to allow attachment.


### 3.4 Cell permeabilisation and transport assay

At ~50% confluence, remove dishes containing cells from the incubator and aspirate the growth media. Permeabilisation of the cell membrane is performed by the following washes, adding the appropriate buffer, waiting for the specified time and then aspirating:

1. Three x 2 ml PBS, 5 min each.

2. One x 2 ml Permeabilisation buffer (PB), 2 min.

3. One x 2.5 ml Digitonin-Permeabilisation buffer (DPB), 10 min.

4. Three x 3 ml Transport buffer (TB), 5 min each.

5. Following permeabilisation the excess buffer can be wicked away using a folded lint-free tissue, before adding the transport reaction mix.

6. Initiate the transport reaction by gently adding 200 μL of import mix onto the cells in the glass bottom dish. If using a labelled cargo, add it here (typical concentrations are 10-50 pM). Wrap the dish in aluminium foil to prevent any photo-conversion or photo-bleaching.

7. If imaging active transport add 1.0 μM RanGDP, alongside Ran Mix and Energy Mix (**See Note 5**)

8. A 1:1000 dilution of 0.1 μm fluorescent beads can be added to the import mix.

9. If fixing the sample, allow the reaction to proceed for 10-20 mins, then apply 2 ml of a 4% paraformaldehyde (PFA in PBS pH 7.4) solution for 15 mins, before washing off and replacing with imaging buffer (**See Note 6**).

10. Image acquisition should start immediately.


### 3.5 Image acquisition and processing


#### 3.5.1 General imaging scheme

Since the equatorial plane of the nucleus of HeLa cells can be 3-7 μm above the coverglass (and hence the fiducial markers used for image registration are out of focus), image acquisition is performed as a sequence (as shown schematically in **Fig 4**), alternating the focus between the imaging plane at equator of the nucleus and the fiducial markers at the

surface of the coverslip.  This acquisition scheme utilizes the laser focus-lock to maintain the focus at each plane to within ±5 nm, and uses the fiducial marker trajectories to perform drift correction post acquisition.  EMCCD cameras are used in kinetic frame transfer mode, with cooling (-80°C), EM "real" gain (typically 500-750) and short exposure times (10-30 ms). Imaging is performed as follows:

1. Wear protective eyewear while operating the microscope.
2. Put a drop of oil on the objective and mount the sample on the stage (**See Note 7**).
3. Verify that the imaging laser is collimated out of the objective by looking at the projection on the ceiling. Adjust the translation of the imaging laser to achieve highly inclined illumination.
4. Focus on the fluorescent beads adsorbed onto the coverglass surface.
5. Determine the relative z-displacement (ΔZ) of the equatorial imaging plane of the nucleus to the surface beads by measuring the laser return beam offset on the PSD, and nanopositioner z-offset at the two focal planes.  Note that the focus lock system uses the stored PSD offset values to lock the focus.
6. Bleach down the sample if necessary by setting the imaging laser to full power (**See Note 8**)
7. Return the focus to the fiducial marker plane
8. Start the image acquisition Python script:
    a. Engage the focus lock, image for 10-30 seconds using a low laser power (5 mW 488 nm), Disengage the focus lock.
    b. Move up to the equatorial plane (+ΔZ), engage the focus lock, and turn on the imaging laser (e.g. ~150 mW 640 nm for SMLM, <20 mW for tracking) and image for 30-120 s.  The length of this acquisition, and the laser power can be optimized to account for the duration of events to be imaged. Note that lateral drift correction is worse for longer imaging periods (**See Note 9**). Disengage the focus-lock.
    c. Move back down to the fiducial plane (-ΔZ).
    d. Return to (a) unless >20 mins of imaging data has been acquired.
9. Stop the acquisition

### 3.5.2 Localisation of molecules

Under the conditions described, individual fluorophores should be visible (**Fig 4**). Each spot represents the true position of the molecule convolved with the Point Spread Function (PSF) of the microscope, and additive noise. The PSF is equivalent to a probability distribution that defines the co-ordinates of the molecule, where fitting a two-dimensional Gaussian function can approximate the centroid.  In practice, the localisation precision of each molecule refers to how precisely we can define the centre of the PSF, given the magnification and S/N of the

image. Since we use a symmetrical Gaussian function to model the PSF, the mean-squared positional error is given by:

$$\sigma_{x,y}^2 \approx \frac{s^2 + \frac{a^2}{12}}{N_m} + \frac{4\sqrt{\pi}s^3 b_m^2}{aN_m^2}$$

where $s$ is the standard deviation of the PSF, $a$ is the pixel size in the image, $N_m$ is the total number of photons measured from the molecule $m$, and $b_m$ is the number of background photons measured in the localisation window [36]. We calculate the photon conversion factor for our camera by measuring the mean and variance of the camera response counts as a function of illumination intensity. In general, the greater the number of photons, the more precise the fit is, so good localisation can depend on using fluorescent molecules that emit many photons (**See Note 2**).

### 3.5.3 Drift Correction

Thermal and mechanical drift is a major problem in long timescale (>mins), single-molecule imaging experiments. During acquisition, drift arising from movement of the stage (lateral) or objective turret or sample (axial/focus drift) can lead to blurry or incorrectly aligned images. Focus drift is corrected using the focus-locking mechanism described earlier, typically to within ±5 nm. Translational drift of the sample is corrected post acquisition using the image data taken from the coverglass immobilised fiducial markers. The protocol for drift correction is as follows:

1. Use the software to identify at least three fiducial markers close to the cell of interest
2. Track these particles over time, and interpolate the trajectory where necessary
3. Overlay all of the trajectories and create a mean trajectory (drift vector)
4. Assess the width of the distribution of the each fiducial trajectory minus the drift vector
5. Discard those with few time points or where there is significant deviation from the drift vector
6. Iteratively refine by repeating steps 1-5
7. Correct the localisation data by subtracting the time dependent drift vector

### 3.5.4 Image creation

A final diffraction-limited image can be reconstructed by summing the images from the acquisition. Generating a two-dimensional histogram of the localisation data can create a final, super-resolved, image. Typically a bin size approximating the localisation precision is used.

1. Run `localisation_image.m` from NPC-localisation-tools to bin-sort the data, using a bin size $h$, corresponding to the localization precision of the instrument.

2. The bin-sorting algorithm also maintains a hash map that maps the bin to the set of localisations found in this bin. This can be used for fast look-up in single-particle analysis.

### 3.6 Single-particle analysis

In order to create a composite map of NTR or cargo localizations in a canonical NPC structure, we first extract the positions of putative NPC complexes found at the nuclear envelope (**Fig 5, See Note 10**). All parameters for the single-particle analysis can be set using the **options.m** file.

1. First, define the nuclear envelope (NE) as a series of vectors, in the 2-dimensional plane of our image, describing a closed curve, arranged in a clockwise direction. The directionality of the curve is important as this allows one to calculate the orientation of the surface normal vector according to the right hand rule. This orientation directly relates to the nucleocytoplasmic axis vector of the NPC.

2. The software passes a scanning window, corresponding to a rotated rectangle whose long axis is aligned with the surface normal vector, along the envelope curve in order to calculate the number of localisations as a function of position on the envelope curve. Let **X** be the set of $n$ single-molecule localisations $x_1,\ldots,x_n$. Let P be a rectangle with four vertices, width $w$ and length $l$, centred at point $p_0$, rotated by some angle relative to the origin, $\theta$ and found on the envelope curve. Polygon P is defined in terms of the unit tangent, **t** and normal, **n** vectors (**Fig 5d**). The width and length parameters are chosen such that the width is approximately that of the feature we are interested in, and the length to be several times that of the feature, to allow refinement of the axial centroid later. We can define a subset **Y** of all localisations, falling within this window. In practice, we can dramatically increase the speed of this calculation by not testing every member of **X** and restricting the set of localisations used to calculate window occupancy to those within a reasonable distance from point $p_0$, using a hash map.

3. Utilising the hash-map and the scanning window, calculate a linearised histogram of localisations along the NE vector by calculating the cardinality of the subset |**Y**| (i.e. the number of localisations within the scanning window). The software will identify peaks within this distribution (utilising peak height, width and separation as control parameters), which correspond to candidate complexes.

Once we have identified the centroids of candidate NPCs along the envelope vector, we can extract and rotationally align the point clouds. This rotational alignment assures that each candidate NPC structure maintains its cytoplasm-to-nucleus orientation vector, but assumes that the NPC is orientated normally to the envelope vector.

1. Using a common axis $\mathbf{c} = [0, 1]^{\mathrm{T}}$ to determine the angle of the rotated box as $\theta = \arccos(\mathbf{n} \cdot \mathbf{c})$, the software will rotate the point cloud of localisations found within the box into the new common axis using a Euclidean transform in homogeneous coordinates:

$$\begin{bmatrix} x' \\ y' \\ 1 \end{bmatrix} = \begin{bmatrix} \cos\theta & -\sin\theta & -p_x \\ \sin\theta & \cos\theta & -p_x \\ 0 & 0 & 1 \end{bmatrix} \begin{bmatrix} x \\ y \\ 1 \end{bmatrix}$$

2. Once we have rotationally aligned data sets to a common axis, we create small images of each pore, again by bin-sorting the data with an appropriate coarseness, $h$. At all points in the following procedure, the mapping between the original point cloud and the discretized (image) version is maintained.

3. Next, each small image is convolved with a radially symmetric two-dimensional Gaussian function in order to smooth the image and facilitate alignment. These smoothed images can then be aligned using a normalised cross-correlation method, or the original point clouds can be aligned using an Iterative Closest Point algorithm (ICP).

4. Specify a suitable template image, and calculate the translational offset of each image in the set relative to the template. Use this offset to align the original point cloud of each structure.

5. Once all of the structures have been aligned, remove those with very large displacements or poor correlation with the remaining data set.

6. Assemble a mean image from the aligned structures.

7. The performance of the alignment procedure can be assessed utilizing synthetic images. Run **`demo.m`** from NPC-localisation-tools.


## 4. Notes

1. Different lasers can be utilised for different experimental geometries. For example the 640 nm laser is often used for *d*STORM type experiments using Alexa647 as a reporter, while the 561 nm laser for PALM experiments, using mEOS as a reporter. In both cases, the 405 nm laser can be used to photo-convert/activate depending on the fluorophore used. By tuning the 405 nm laser power, the amount of photoactivation/conversion can be tightly controlled. The 488 nm laser is often used for semiconductor nanocrystal tracking experiments (SPT) or for visualising GFP constructs.

2. Additionally, by inserting an aperture in a conjugate plane to the specimen plane (with the appropriate relay lenses), the system can be also used for true HILO illumination.

3. Several commercial focus-lock systems are available from major microscope manufacturers. There are also several open source solutions such as PGFocus (http://big.umassmed.edu/wiki/index.php/PgFocus). Here we utilise our own, since it is cheap and highly customisable for the acquisition protocol.

4. For SMLM, dyes such as Alexa647 show ideal photo-physical properties (blinking, quantum yield *etc.*). Semiconductor nanocrystals such as Quantum Dots can be utilised to create synthetic cargos capable of being tracked for minutes. However, these particles are larger in size than synthetic moieties or fluorescent proteins. In some cases this precludes them from use for particular types of SPT experiments.

5. Once the cells have been permeabilised and the cytoplasm washed out, the RanGTP gradient has been abolished. The Ran and Energy Mixes therefore contain all of the components required to re-initialise and maintain the RanGTP gradient within the permeabilised cells, and therefore permit active transport. This should be tested using model cargos.

6. The imaging buffer is an oxygen scavenging system to remove oxygen and thus preventing photobleaching. The buffer also contains an appropriate amount of reducing agent (typically β-Mercaptoethanol or β-Mercaptoethylamine) that promotes the blinking required for SMLM or indeed can reduce blinking in nanocrystal tracking experiments. Care needs to be taken over the pH of the buffer, as it will decay over time. Also, some commercially available buffers have a high refractive index that may interfere with the use of the focus-lock system.

7. Sample drift is often most pronounced at the beginning of the experiment, and generally immediately after the sample is mounted on the microscope. To minimize the amount of drift observed in the experiment, let the sample settle for a period of minutes before beginning the acquisition.

8. For SMLM it can be advisable to "bleach down" the sample, using a high-laser power, prior to acquisition to ensure that single fluorophores are visible and sparse. Many localisation algorithms can generate artefacts if the data are not sparse.

9. There exists a trade-off between observing longer interactions and the accuracy of registration using the drift correction. Longer interactions require a longer period of imaging, during which the fiducial markers cannot easily be tracked.

10. Labelling a second component of the NPC, such as POM-121 or Nup358, with a second dye, can be used to verify the identity and orientation of putative NPCs.

**Acknowledgements**
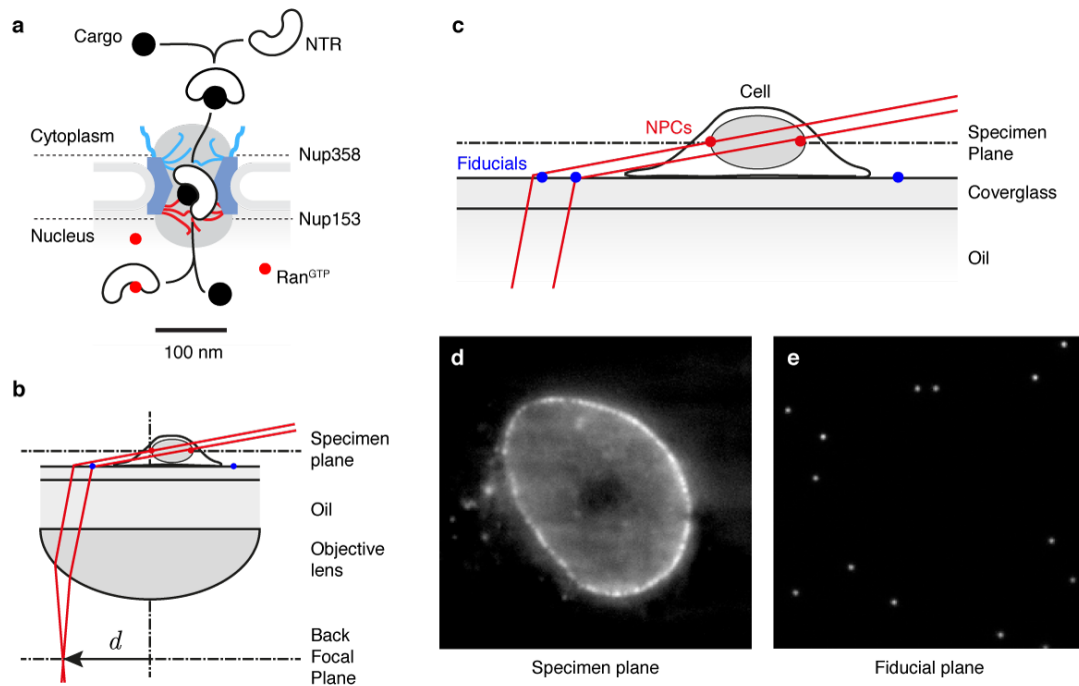
**FIGURES**



**Figure 1 | Schematic describing simplified NPC transport mechanism and imaging assay to probe cargo/NTR interactions. (a)** A simplified schematic describing active import of cargos into the nucleus.  A cargo bearing a Nuclear Localisation Signal (NLS), must bind to cognate Nuclear Transport Receptors (NTRs) enabling the cargo to enter into the NPC.  A sharp spatial gradient of the GTP form of Ran GTPase provides the directionality to active transport. The scale bar refers to the NPC structure rather than the soluble components (Cargo, NTRs and Ran).  **(b)** Illumination setup to increase imaging signal-to-noise.  Rather than standard epifluorescence illumination the laser can be inclined through the sample, by introducing an offset, $d$, in the position of the imaging laser at the BFP of the objective. Additionally, adding a slit in the conjugate plane to the specimen plane (HILO) can improve S/N further.  **(c)** Schematic showing the two focal planes which must be imaged, the specimen plane containing the NPCs, and the fiducial plane where fluorescent beads can be utilised to correct lateral drift.  **(d)** Example of a HILO image of labelled NTRs interacting with the NPC.  Individual NPCs can be identified as discrete puncta. **(e)** Example widefield image of fluorescent beads localised to the surface of the glass coverslip.
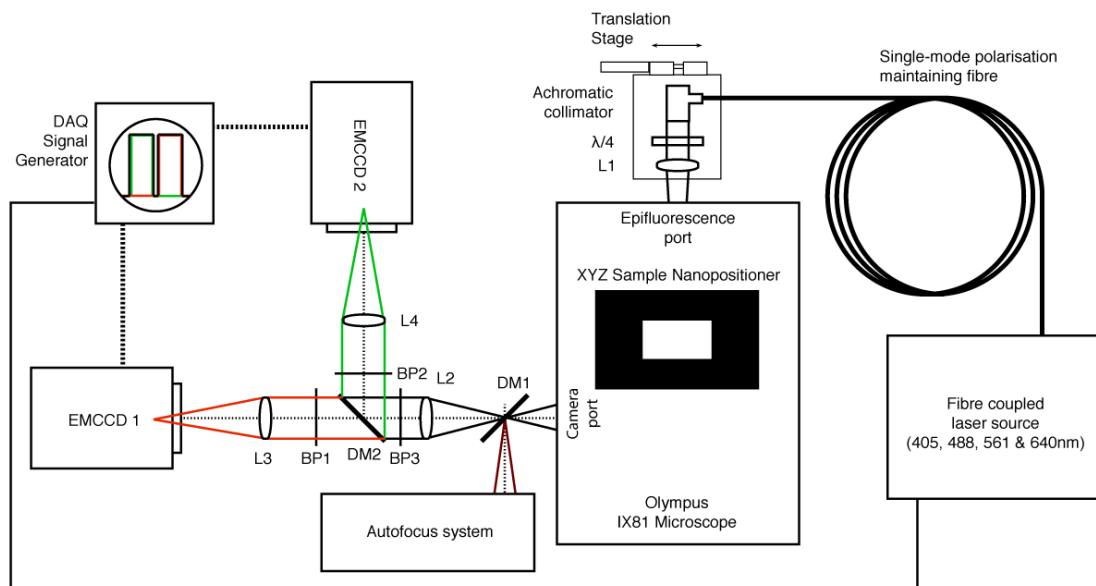
**Figure 2 | Schematic of single-molecule localisation microscope optical layout.** An Olympus IX81 base with high NA objective is used as the body of the microscope. Laser illumination is coupled into the system using a single-mode fibre. Two EMCCD cameras are attached to the camera port via a relay, enabling simultaneous two-colour imaging. Cameras and lasers are synchronised using an external signal generator. An infrared laser autofocus system is coupled via the camera port to maintain a focus lock during image acquisition.
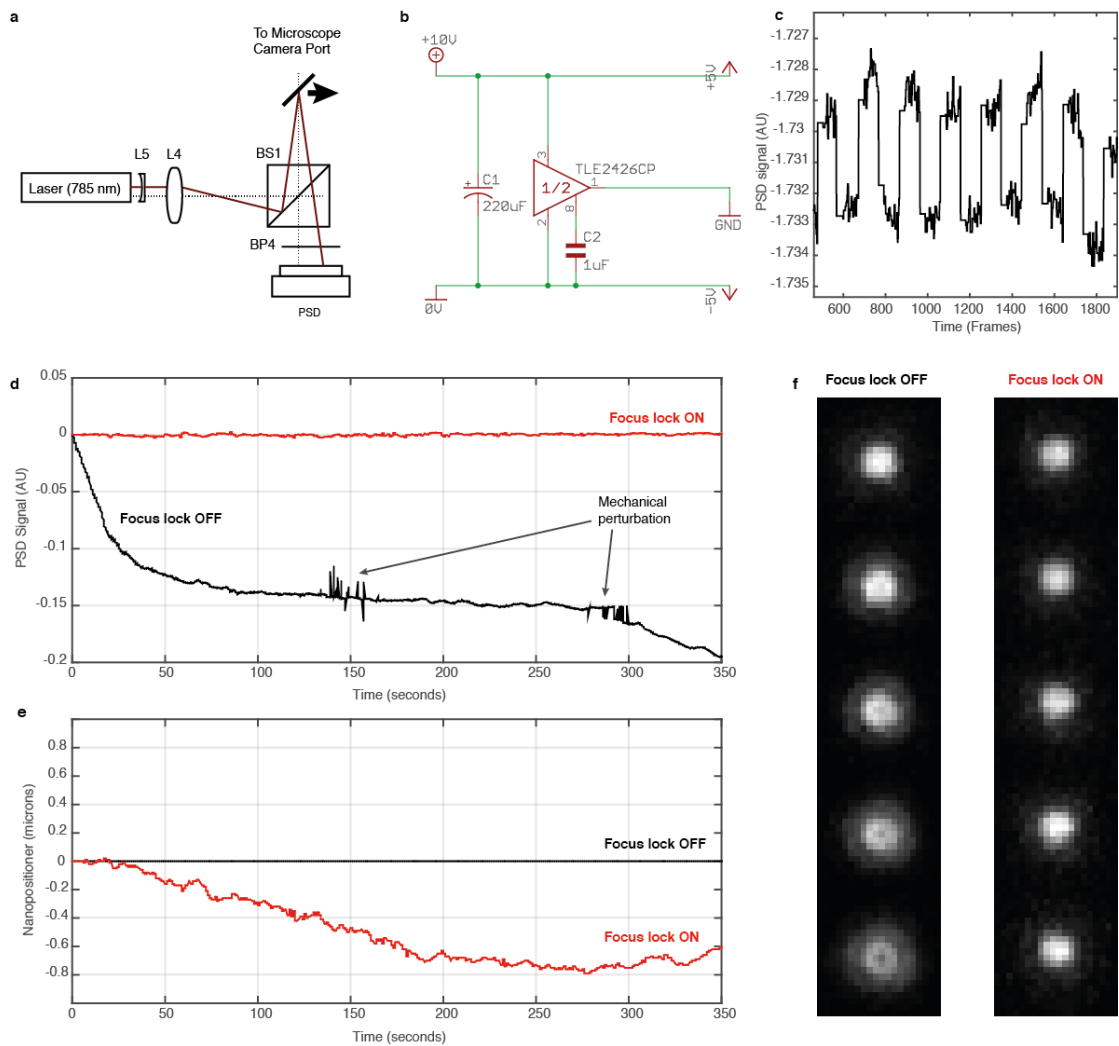
**Figure 3 | Real-time focus locking system employed to maintain the imaging plane in focus. (a)** Optical layout of total internal reflection of a near IR laser onto a position sensitive detector via the camera port of the microscope. **(b)** Low cost bipolar power supply design for the PSD. **(c)** Readout of PSD with 1Hz, 50 nm square-wave applied to the nanopositioner. **(d)** PSD signal of sample with the focus-locking device either on or off. With the focus-lock off, the PSD signal rapidly decreases, corresponding to the mechanical drift of the objective turret. With the focus-lock engaged, the PSD signal stays constant. **(e)** Output of the PID control loop to the nanopositioner with the focus lock engaged, shows the corrections applied to the system to maintain focus. **(f)** Images of 100 nm fluorescent fiducal markers as a function of time with the focus lock off and on, demonstrating maintenance of the focus.
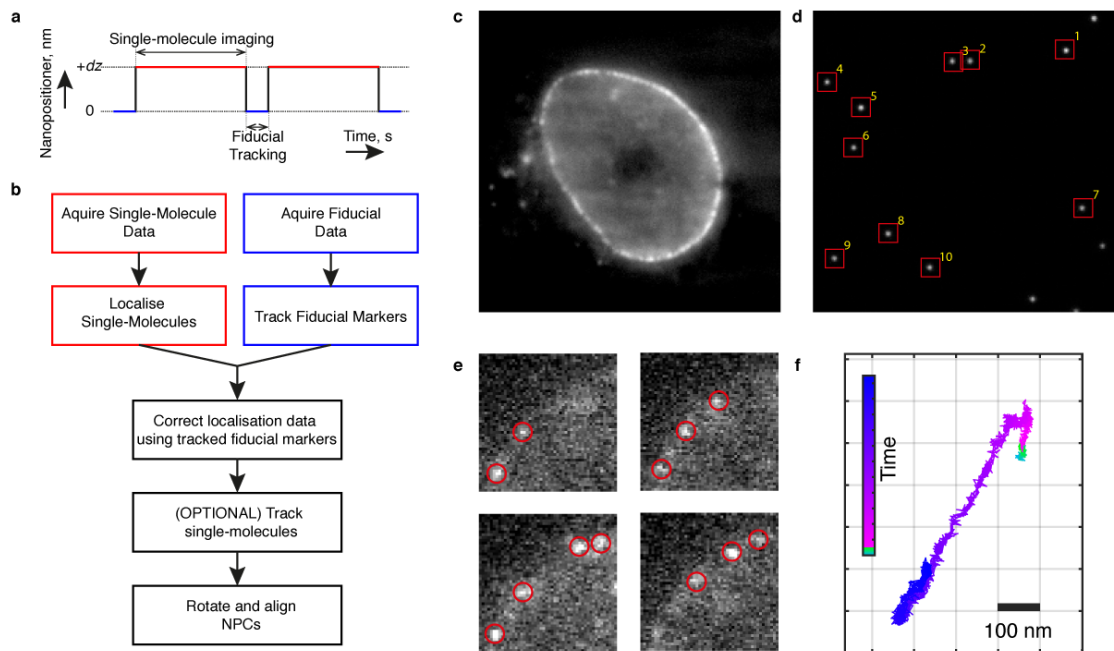
**Figure 4 | Data acquisition and processing workflow. (a)** Scheme for sequentially imaging two planes within the sample, the specimen plane and the fiducial plane. The nanopositioner (using feedback from the focus lock) maintains the position at either of the two planes. **(b)** Generalised method workflow describing the data acquisition and processing steps. **(c)** An example HILO image of a nucleus labelled with NTRs. Individual puncta are evident at the nuclear envelope. **(d)** Widefield image of fiducial markers at the coverglass surface. Software is used to identify the particles. **(e)** Raw frames from a live single-molecule tracking experiment showing individual molecules. Each molecule is localised in each frame. **(f)** Example fiducial marker trajectory from a long imaging acquisition showing an example of translational drift during acquisition.
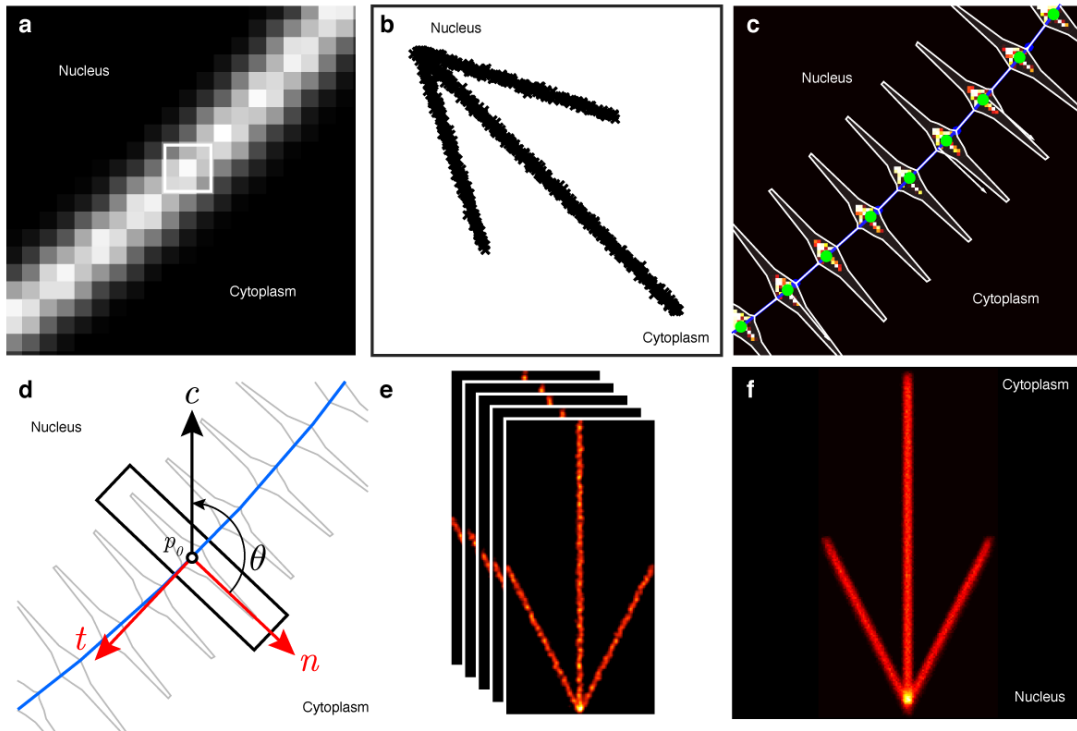
**Figure 5 | Single-particle analysis of SMLM microscopy data.** This figure uses simulated data where NPCs are represented as directional arrows arranged along an envelope structure. **(a)** Simulated diffraction limited image of arrow structures arranged at an envelope. **(b)** Example of the underlying localisations representing the arrow structure highlighted in (a). **(c)** After having drawn (or fit) the envelope vector (blue line), the software generates an envelope histogram with putative NPC structures marked with green dots. **(d)** Geometry of the alignment transformation. Three vectors are shown, $c$ the unit alignment vector, $t$, the envelope tangent vector and $n$, the orientation vector of the putative NPC centred at point $p_0$. The structure is extracted and rotated by the angle $\theta$ to bring all structures into register. **(e)** Examples of individual structures to be aligned. **(f)** Mean image of aligned structures, following cross-correlation or ICP based alignment from (e).

## References

1. Devos D, Dokudovskaya S, Williams R, Alber F, Eswar N, Chait BT, Rout MP, Sali A (2006) Simple fold composition and modular architecture of the nuclear pore complex. Proc Natl Acad Sci U S A 103 (7):2172-2177. doi:10.1073/pnas.0506345103

2. Grossman E, Medalia O, Zwerger M (2012) Functional architecture of the nuclear pore complex. Annu Rev Biophys 41:557-584. doi:10.1146/annurev-biophys-050511-102328

3. Terry LJ, Shows EB, Wente SR (2007) Crossing the nuclear envelope: hierarchical regulation of nucleocytoplasmic transport. Science 318 (5855):1412-1416. doi:10.1126/science.1142204

4. Kalderon D, Roberts BL, Richardson WD, Smith AE (1984) A short amino acid sequence able to specify nuclear location. Cell 39 (3 Pt 2):499-509

5. Cingolani G, Petosa C, Weis K, Müller CW (1999) Structure of importin-beta bound to the IBB domain of importin-alpha. Nature 399 (6733):221-229. doi:10.1038/20367

6. Ribbeck K, Görlich D (2001) Kinetic analysis of translocation through nuclear pore complexes. EMBO J 20 (6):1320-1330. doi:10.1093/emboj/20.6.1320

7. Izaurralde E, Kutay U, von Kobbe C, Mattaj IW, Gorlich D (1997) The asymmetric distribution of the constituents of the Ran system is essential for transport into and out of the nucleus. EMBO J 16 (21):6535-6547. doi:10.1093/emboj/16.21.6535

8. Kalab P, Weis K, Heald R (2002) Visualization of a Ran-GTP gradient in interphase and mitotic Xenopus egg extracts. Science 295 (5564):2452-2456. doi:10.1126/science.1068798

9. Görlich D, Panté N, Kutay U, Aebi U, Bischoff FR (1996) Identification of different roles for RanGDP and RanGTP in nuclear protein import. The EMBO Journal 15 (20):5584-5594

10. Rout MP, Aitchison JD, Magnasco MO, Chait BT (2003) Virtual gating and nuclear transport: the hole picture. Trends Cell Biol 13 (12):622-628

11. Frey S, Richter RP, Görlich D (2006) FG-rich repeats of nuclear pore proteins form a three-dimensional meshwork with hydrogel-like properties. Science 314 (5800):815-817. doi:10.1126/science.1132516

12. Frey S, Görlich D (2007) A saturated FG-repeat hydrogel can reproduce the permeability properties of nuclear pore complexes. Cell 130 (3):512-523. doi:10.1016/j.cell.2007.06.024

13. Lowe AR, Tang JH, Yassif J, Graf M, Huang WY, Groves JT, Weis K, Liphardt JT (2015) Importin-β modulates the permeability of the nuclear pore complex in a Ran-dependent manner. Elife 4. doi:10.7554/eLife.04052

14. Bestembayeva A, Kramer A, Labokha AA, Osmanović D, Liashkovich I, Orlova EV, Ford IJ, Charras G, Fassati A, Hoogenboom BW (2015) Nanoscale stiffness topography reveals structure and mechanics of the transport barrier in intact nuclear pore complexes. Nat Nanotechnol 10 (1):60-64. doi:10.1038/nnano.2014.262

15. Adam SA, Marr RS, Gerace L (1990) Nuclear protein import in permeabilized mammalian cells requires soluble cytoplasmic factors. The Journal of Cell Biology 111 (3):807-816

16. Dange T, Grünwald D, Grünwald A, Peters R, Kubitscheck U (2008) Autonomy and robustness of translocation through the nuclear pore complex: a single-molecule study. J Cell Biol 183 (1):77-86. doi:10.1083/jcb.200806173

17. Yang W, Musser SM (2006) Nuclear import time and transport efficiency depend on importin beta concentration. The Journal of cell biology 174 (7):951-961. doi:10.1083/jcb.200605053

18. Kubitscheck U, Grünwald D, Hoekstra A, Rohleder D, Kues T, Siebrasse JP, Peters R (2005) Nuclear transport of single molecules: dwell times at the nuclear pore complex. J Cell Biol 168 (2):233-243. doi:10.1083/jcb.200411005

19. Kahms M, Lehrich P, Hüve J, Sanetra N, Peters R (2009) Binding site distribution of nuclear transport receptors and transport complexes in single nuclear pore complexes. Traffic 10 (9):1228-1242. doi:10.1111/j.1600-0854.2009.00947.x

20. Tokunaga M, Imamoto N, Sakata-Sogawa K (2008) Highly inclined thin illumination enables clear single-molecule imaging in cells. Nat Methods 5 (2):159-161. doi:10.1038/nmeth1171

21. Ma J, Yang W (2010) Three-dimensional distribution of transient interactions in the nuclear pore complex obtained from single-molecule snapshots. Proc Natl Acad Sci U S A 107 (16):7305-7310. doi:10.1073/pnas.0908269107

22. Yang W (2013) Distinct, but not completely separate spatial transport routes in the nuclear pore complex. Nucleus 4 (3):166-175. doi:10.4161/nucl.24874

23. Lowe AR, Siegel JJ, Kalab P, Siu M, Weis K, Liphardt JT (2010) Selectivity mechanism of the nuclear pore complex characterized by single cargo tracking. Nature 467 (7315):600-603. doi:10.1038/nature09285

24. Sun C, Yang W, Tu LC, Musser SM (2008) Single-molecule measurements of importin alpha/cargo complex dissociation at the nuclear pore. Proc Natl Acad Sci U S A 105 (25):8613-8618. doi:10.1073/pnas.0710867105

25. Betzig E, Patterson GH, Sougrat R, Lindwasser OW, Olenych S, Bonifacino JS, Davidson MW, Lippincott-Schwartz J, Hess HF (2006) Imaging Intracellular Fluorescent Proteins at Nanometer Resolution. Science (New York, NY) 313 (5793):1642-1645. doi:10.1126/science.1127344

26. Rust M, Bates M, Zhuang X (2006) Sub-diffraction-limit imaging by stochastic optical reconstruction microscopy (STORM). Nature methods 3 (10):793-796

27. Heilemann M, van de Linde S, Mukherjee A, Sauer M (2009) Super-resolution imaging with small organic fluorophores. Angew Chem Int Ed Engl 48 (37):6903-6908. doi:10.1002/anie.200902073

28. Löschberger A, van de Linde S, Dabauvalle MC, Rieger B, Heilemann M, Krohne G, Sauer M (2012) Super-resolution imaging visualizes the eightfold symmetry of gp210 proteins around the nuclear pore complex and resolves the central channel with nanometer resolution. J Cell Sci 125 (Pt 3):570-575. doi:10.1242/jcs.098822

29. Löschberger A, Franke C, Krohne G, van de Linde S, Sauer M (2014) Correlative super-resolution fluorescence and electron microscopy of the nuclear pore complex with molecular resolution. J Cell Sci 127 (Pt 20):4351-4355. doi:10.1242/jcs.156620

30. Szymborska A, de Marco A, Daigle N, Cordes VC, Briggs JA, Ellenberg J (2013) Nuclear pore scaffold structure analyzed by super-resolution microscopy and particle averaging. Science 341 (6146):655-658. doi:10.1126/science.1240672

31. Henriques R, Lelek M, Fornasiero EF, Valtorta F, Zimmer C, Mhlanga MM (2010) QuickPALM: 3D real-time photoactivation nanoscopy image processing in ImageJ. Nat Methods 7 (5):339-340. doi:10.1038/nmeth0510-339

32. Ovesny M, Krizek P, Borkovec J, Svindrych Z, Hagen GM (2014) ThunderSTORM: a comprehensive ImageJ plug-in for PALM and STORM data analysis and super-resolution imaging. Bioinformatics 30 (16):2389-2390. doi:10.1093/bioinformatics/btu202

33. Starr R, Stahlheber S, Small A (2012) Fast maximum likelihood algorithm for localization of fluorescent molecules. Optics Letters 37 (3):413-415

34. Crocker… J (1996) Methods of digital video microscopy for colloidal studies. … of Colloid and Interface Science

35. Jaqaman K, Loerke D, Mettlen M, Kuwata H, Grinstein S, Schmid SL, Danuser G (2008) Robust single-particle tracking in live-cell time-lapse sequences. Nature methods 5 (8):695-702. doi:10.1038/nmeth.1237

36. Thompson R, Larson D, Webb W (2002) Precise nanometer localization analysis for individual fluorescent probes. Biophysical Journal 82 (5):2775-2783